Article

Synergistic Catalysis of SnO$_2$/Reduced Graphene Oxide for VO^{2+}/VO$_2^+$ and V^{2+}/V^{3+} Redox Reactions

Yongguang Liu, Yingqiao Jiang, Yanrong Lv, Zhangxing He *, Lei Dai and Ling Wang *

School of Chemical Engineering, North China University of Science and Technology, Tangshan 063009, China; hglyg@ncst.edu.cn (Y.L.); jiangying_qiao@163.com (Y.J.); yronglv@163.com (Y.L.); dailei_b@163.com (L.D.)
* Correspondence: zxhe@ncst.edu.cn (Z.H.); tswling@126.com (L.W.); Tel./Fax: +86-315-2592170 (Z.H.)

Abstract: In spite of their low cost, high activity, and diversity, metal oxide catalysts have not been widely applied in vanadium redox reactions due to their poor conductivity and low surface area. Herein, SnO$_2$/reduced graphene oxide (SnO$_2$/rGO) composite was prepared by a sol–gel method followed by high-temperature carbonization. SnO$_2$/rGO shows better electrochemical catalysis for both redox reactions of VO^{2+}/VO$_2^+$ and V^{2+}/V^{3+} couples as compared to SnO$_2$ and graphene oxide. This is attributed to the fact that reduced graphene oxide is employed as carbon support featuring excellent conductivity and a large surface area, which offers fast electron transfer and a large reaction place towards vanadium redox reaction. Moreover, SnO$_2$ has excellent electrochemical activity and wettability, which also boost the electrochemical kinetics of redox reaction. In brief, the electrochemical properties for vanadium redox reactions are boosted in terms of diffusion, charge transfer, and electron transport processes systematically. Next, SnO$_2$/rGO can increase the energy storage performance of cells, including higher discharge electrolyte utilization and lower electrochemical polarization. At 150 mA cm^{-2}, the energy efficiency of a modified cell is 69.8%, which is increased by 5.7% compared with a pristine one. This work provides a promising method to develop composite catalysts of carbon materials and metal oxide for vanadium redox reactions.

Keywords: vanadium redox reaction; electrochemical kinetics; SnO$_2$/reduced graphene oxide; catalyst

1. Introduction

With the development of industrial processes, energy consumption is increasing day by day. However, energy consumption brings environmental pollution [1–4]. In order to solve this problem and achieve "carbon neutrality", humankind began to explore renewable energy [5–9]. However, this type of energy is not always available at all times, and in most cases, due to the oscillation of energy availability in its cycle and peak demand, supply and demand are not synchronized [10–15]. Energy storage equipment is needed to store and transform the electric energy generated by renewable energy sources to realize its large-scale application [16–20]. Among many energy storage devices, a vanadium redox flow battery (VRFB) has attracted much attention because of its unique performance [21–23]. The main components of a VRFB are electrodes, electrolytes, and proton exchange membranes [24–26]. The performance of an electrode has a direct impact on the overall performance of the battery. Carbon-based materials have become the most widely used electrode material in a VRFB due to their large specific surface area and good corrosion resistance. However, the electrochemical performance of carbon-based materials is poor, which is not conducive to their large-scale utilization. In order to improve the performance of carbon-based materials and expand the use of materials, researchers have modified them. Common electrode modification methods mainly include intrinsic treatment and the introduction of catalysts.

There are several categories of catalysts, including carbon materials, metal, metal oxide, metal nitride, metal boride, and metal carbide. Firstly, carbon materials (CNTs,

graphene, carbon sheet, carbon nanofiber, etc.) have advantages including a low cost, obvious structure, and a larger surface area, and have been widely used as a catalyst in VRFB [27–29]. For example, Yan et al. [30] developed multi-walled carbon nanotubes as a catalyst for VO^{2+}/VO_2^+ redox reaction. In addition, some biomass-based carbon materials derived from glucose, fish scales, and kiwi fruit have abundant groups, heteroatoms, and a large surface area, which also show certain electrochemical catalysts for a vanadium redox reaction [31,32]. Metal has a unique atomic structure and high conductivity, and exhibits intrinsic catalysis for a vanadium redox reaction. Metal catalysts mainly include Au, Pt, Ir, Cu, etc. Zeng et al. [33] used a copper nanoparticle to decorate graphite felt with in situ electrodeposition. The copper nanoparticle was an excellent catalyst for a V^{3+}/V^{2+} redox reaction, and improved the energy efficiency of the VRFB. However, most of the metal catalysts have disadvantages, including a high price and easy access to hydrogen evolution. Moreover, metal oxides have attracted more attention due to the advantages of a low cost, high stability, and diversity. In recent decades, many metal oxides including ZrO_2, TiO_2, CeO_2, WO_3, SnO_2, etc., have been developed and applied in VRFB [34–39]. For instance, Chen et al. [35] modified graphite felt with a ZrO_2 nanoparticle by thermal decomposition. ZrO_2 showed good wettability and acted as active sites for both redox reactions, resulting in faster mass and charge transfer processes. However, due to the low conductivity, the intrinsic catalysis of metal oxide is not efficiently used. Other metal compounds have been developed as catalysts for VRFB. For example, the $Ti_3C_2T_x$ MXene spheres have metallic behavior and a high electrical conductivity, which shows high catalysis for a V^{3+}/V^{2+} redox reaction [40]. Moreover, metal borides such as TiB_2 and ZrB_2 exhibit high conductivity for a V^{3+}/V^{2+} redox reaction [41,42]. It is noteworthy that carbon materials can be used as support to not only improve conductivity of metal oxide but also to increase the surface area of metal oxide. Therefore, it is an efficient way to obtain high-performance catalysts by compositing carbon materials and metal oxide. For example, Li et al. [43] synthesized a polydopamine-Mn_3O_4 composite as a catalyst for a VO^{2+}/VO_2^+ redox reaction. The synergistic effect of polydopamine and Mn_3O_4 improved the electrochemical performance of the VRFB.

SnO_2 is an amphoteric oxide, which can exist stably in the strong acidic environment of a VRFB electrolyte [39,44]. Due to the wide band gap and unique performance of SnO_2, it is widely used in optics, sensors, and other fields [45]. A large number of experiments have proved that SnO_2 has a good catalytic effect on V^{3+}/V^{2+} and VO_2^+/VO^{2+} redox reactions. Ha et al. [39] prepared in situ SnO_2 nanoparticles and modified carbon felt electrodes by the hydrothermal method. SnO_2 reduced the activation potential of the reaction and increased the reaction rate. The SnO_2 modified electrode significantly improves the stability of the battery, which is very important for the VRFB. Graphene has good electrical conductivity, high stability, and a large surface area, making it an excellent electrocatalyst carbon support. Walsh et al. [46] studied the synergy between graphene and Mn_3O_4. Due to the interaction between graphene support and the Mn_3O_4 catalyst, the catalytic performance of the composite material is higher than that of any component alone.

In this article, we used SnO_2 as the electrocatalyst and reduced graphene oxide as the carbon support, respectively. The large surface area of reduced graphene oxide not only makes the SnO_2 nanoparticle more dispersive, but also provides a larger reaction place for redox reaction. In addition, the high conductivity of reduced graphene oxide boosts the transport of electrons for redox reaction. Therefore, it is inferred that the synergetic effect between reduced graphene oxide and SnO_2 is more conducive to a vanadium redox reaction. The catalytic performance of the SnO_2/reduced graphene oxide composite catalyst for V^{3+}/V^{2+} and VO_2^+/VO^{2+} reactions is much higher than using SnO_2 and reduced graphene oxide alone as a catalyst. Due to the synergy between SnO_2 and reduced graphene oxide, the composite catalyst has good electrochemical activity and stability.

2. Experimental

2.1. Preparation of Materials

As shown in Figure 1, the sample was prepared by the sol–gel method. First, 1.4977 g of $SnCl_2 \cdot 2H_2O$ was weighed and placed in a beaker. Then, 13.27 mL of an anhydrous ethanol/water mixed solution (volume ratio: 15:1) was added and stirred in a water bath at 65 °C for 40 min to gradually form a gel. After the gel was formed, it was aged in air for 24 h to obtain a precursor of tin sol. Then, 50 mg of graphene oxide (GO), the tin sol precursor, and 10 mL of anhydrous alcohol were mixed and ultrasonically dispersed for 1 h. Next, the sample was placed in a drying oven to dry adequately at 80 °C. The Ar was put into the tube furnace before calcining for 2 h to exhaust the air. Then, the sample was calcined at 500 °C for 2 h. The obtained sample was named as SnO_2/rGO.
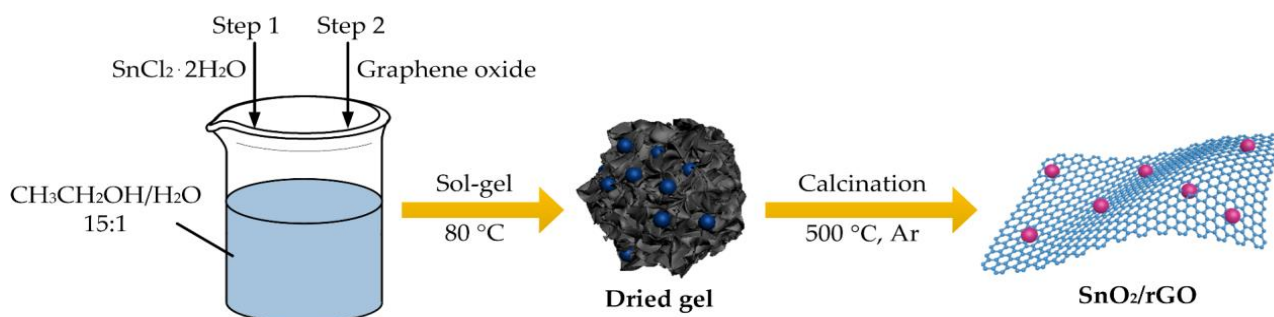
Figure 1. Illustration of preparation procedure of SnO_2/rGO by sol-gel method.

2.2. Characterization of Materials

The crystal phases of the samples were studied using the D8 Advance A25 Instrument (Bruker, Berlin, Germany). The microscopic morphology of the sample was observed by a scanning electron microscope (SEM, JSM-IT100). The internal morphology and crystal lattice of the sample were observed by a transmission electron microscope (TEM, JEOL JEM-2100F). The 3H-2000PM1 specific surface area and porous analyzer was used to analyze the materials surface area. The X-ray photoelectron spectroscopy (XPS) of the samples was studied using the Thermo Scientific Escalab 250Xi instrument (Thermo Fisher Scientific, Waltham, MA, USA) to determine the elemental composition of the samples.

2.3. Electrochemical Measurements

First, 10 mg of the catalyst was thoroughly mixed with 5 mL of N,N-dimethylformamide (DMF) to obtain a dispersion. The dispersion solution was then put into an ultrasonic cleaning machine and dispersed continuously for 3 h, until the catalyst was evenly dispersed in DMF. The dispersion was then dropped on the glassy carbon electrode (GCE) and left to stand at room temperature for 4 h.

Cyclic voltammetry (CV) and electrochemical impedance spectroscopy (EIS) measurements were performed by an electrochemical workstation (CHI660E, Shanghai Chenghua, Shanghai, China). In this three-electrode system, platinum electrode (1×1 cm^2) was the counter electrode, glassy carbon electrode was the working electrode, and the calomel electrode was the reference electrode. Positive and negative CV and EIS tests were accomplished in 1.6 M VO^{2+} + 3.0 M H_2SO_4 and 1.6 M V^{3+} + 3.0 M H_2SO_4, respectively. The voltage scanning range of the CV test for a V^{2+}/V^{3+} reaction was from -0.75 to -0.1 V, and the VO^{2+}/VO_2^+ reaction was from 0.2 to 1.5 V. The frequency range for EIS was 1 to 1×10^6 Hz. The EIS of the VO^{2+}/VO_2^+ and V^{2+}/V^{3+} reactions were tested at the polarization of 0.85 V and -0.45 V, respectively.

2.4. Charge–Discharge Tests

The catalyst modification cell and the pristine cell were assembled to compare the VRFB's performance. CT2001A was used for charge–discharge tests. Graphite felt (3×3 cm^2) was activated in a muffle furnace at 400 °C for 10 h. The activated graphite felt was then dipped into the dispersion solution. The dispersion solution was composed of 3 mg of the catalyst and 10 mL of DMF. After the graphite felt completely absorbed the dispersion solution, it was taken out and dried at 80 °C. The above steps were repeated until the dispersion solution was completely absorbed in order to obtain the SnO$_2$/rGO modify graphite felt electrode.

The SnO$_2$/rGO modify graphite felt was, respectively, used as the positive and negative electrodes of the modified cell. The active graphite felt was used as the pristine cell. The graphite felt was placed in the electrolyte of 0.8 M V^{3+} + 0.8 M VO^{2+} + 3.0 M H$_2$SO$_4$ to fully absorb the electrolyte. The rate performance was tested at 50, 75, 100, 125, and 150 mA cm^{-2} current densities.

## 3. Results and Discussion

Figure 2a–c show the SEM images of GO, SnO$_2$, and SnO$_2$/rGO, respectively. As shown in Figure 2a, GO is curly. Figure 2b shows the SnO$_2$ particles have obvious agglomeration. It can be seen from Figure 2c that SnO$_2$ is evenly distributed on the reduced graphene oxide sheet. As shown in Figure 2d–f, the morphology of the SnO$_2$/rGO composite was further characterized by TEM. The low magnification TEM figure shows that a large amount of SnO$_2$ is loaded on the reduced graphene oxide sheet. There is a large amount of aggregation, which can be seen more clearly from the medium magnification TEM figure. From the high magnification TEM figure, it can be further concluded that the obvious lattice fringes are 0.34 nm, which is the (110) surface of SnO$_2$. Figure 2g, h display the EDX spectra of GO and SnO$_2$/rGO, respectively. Absolutely, SnO$_2$/rGO have C and O. Compared with Figure 2g, there is Sn in Figure 2h. It can be concluded that there is Sn in SnO$_2$/rGO.

Figure 2i shows the X-ray diffraction pattern of the samples. The crystal structure of the samples was studied by XRD. There is a characteristic peak at 12.7° for graphene oxide, which proves that the purity of graphene oxide is very high [47]. The observed pattern of SnO$_2$ is consistent with the standard value (JCPDS: 00-021-1250), and there is no characteristic peak of impurity. The reduced graphene oxide crystallization peaks in the XRD pattern of SnO$_2$/rGO are lack. The order of the reduced graphene oxide plane is disrupted by the SnO$_2$ particles, or reduced graphene oxide sheets are inserted into the SnO$_2$ lattice [48]. SnO$_2$/rGO has the advantages of two materials. It has both the conductivity of rGO and the catalytic performance of SnO$_2$, which can improve the electrochemical catalytic performance.

Figure 3a, b show the N$_2$ adsorption and desorption isotherms of GO and SnO$_2$/rGO. The isotherms of GO and SnO$_2$/rGO are type IV, indicating that the two are mesopores materials. Additionally, the two isotherms exhibit type H3 loops, which identified with plate-like porous aggregates, as these originate from slit-shaped interlayer pores. Based on the multilayer adsorption theory, the specific surface areas of GO and SnO$_2$/rGO were computed to be 44.3 m^2 g^{-1} and 208.9 m^2 g^{-1}, respectively. Pore distribution has been assessed by means of the Barrett–Joyner–Halenda (BJH) method, and the results have been shown in Figure 3c,d. It can be seen that GO and SnO$_2$/rGO contain a large number of mesoporous of ~4 nm. The pore width is not affected by heat treatment. The increase of mesoporous can explain why SnO$_2$/rGO has a larger surface area, which can provide a larger reaction place for electrode reaction.
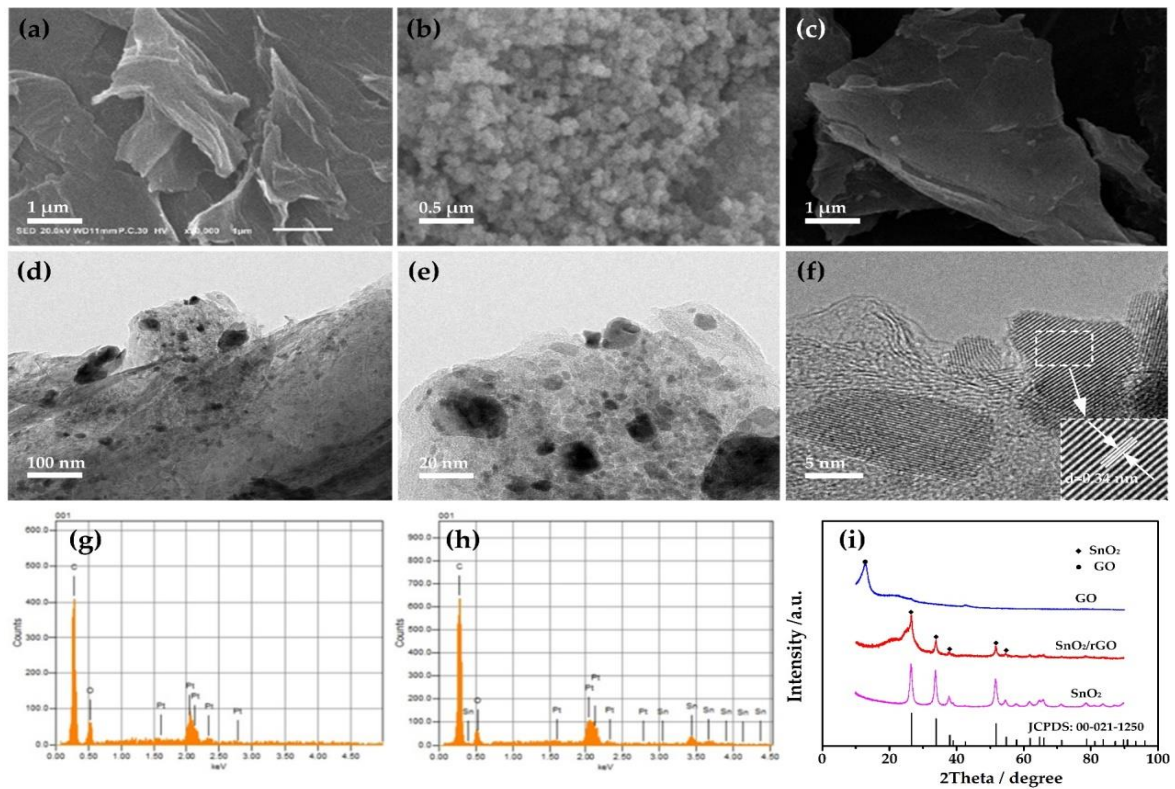
Figure 2. (**a**) SEM image of GO; (**b**) SEM image of SnO_2; (**c**) SEM image of SnO_2/rGO; (**d**,**e**) TEM images; (**f**) high-resolution TEM image of SnO_2/rGO; (**g**) EDX spectra of GO; (**h**) EDX spectra of SnO_2/rGO; (**i**) XRD patterns of all samples.
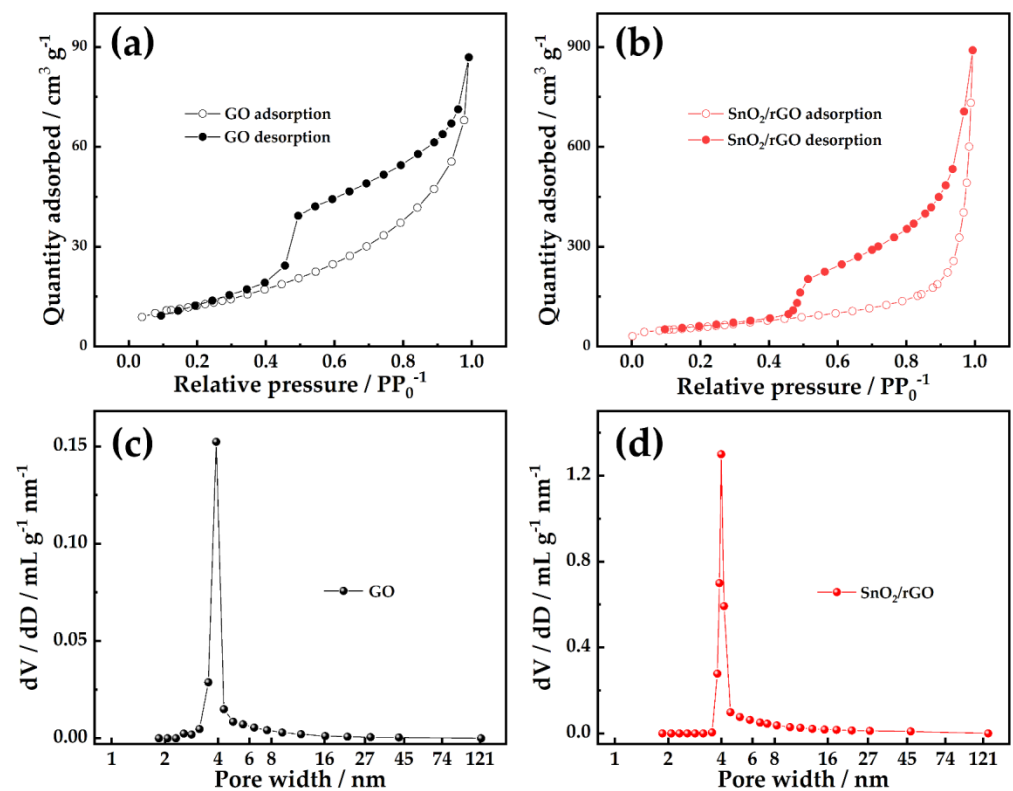

Figure 3. (**a**) N_2 adsorption–desorption isotherms of GO; (**b**) SnO_2/rGO; (**c**) pore-size distributions of GO; (**d**) SnO_2/rGO based on BJH model.

The element composition of SnO_2/rGO was further analyzed by XPS. The XPS spectrum survey of SnO_2/rGO is shown in Figure 4a. It shows that the peaks in the energy spectrum of SnO_2/rGO correspond to C 1s, O 1s, and Sn 3d, indicating that SnO_2/rGO consists of C, O, and Sn elements. Figure 4b–d show the high-resolution XPS spectra of C 1s, O 1s, and Sn 3d, respectively. There are three peaks centered at 284.4, 285.6, and 288.6 eV, which correspond to C-C, C-O, and O-C=O bonds, respectively. These C 1s peaks related to oxygen-containing groups are very weak. The peaks at 531.1 and 532.3 eV shown in Figure 4c correspond to Sn-O and C-O bonds. These binding energies are characteristic of oxygen ionization on the SnO_2 surface. Figure 4d shows two different peaks with binding energies of 487.0 and 495.4 eV, corresponding to Sn $3d_{5/2}$ and Sn $3d_{3/2}$, respectively. This indicates the presence of Sn^{4+} and the formation of SnO_2 [49]. It can be concluded that SnO_2/rGO is composed of reduced graphene oxide and SnO_2.
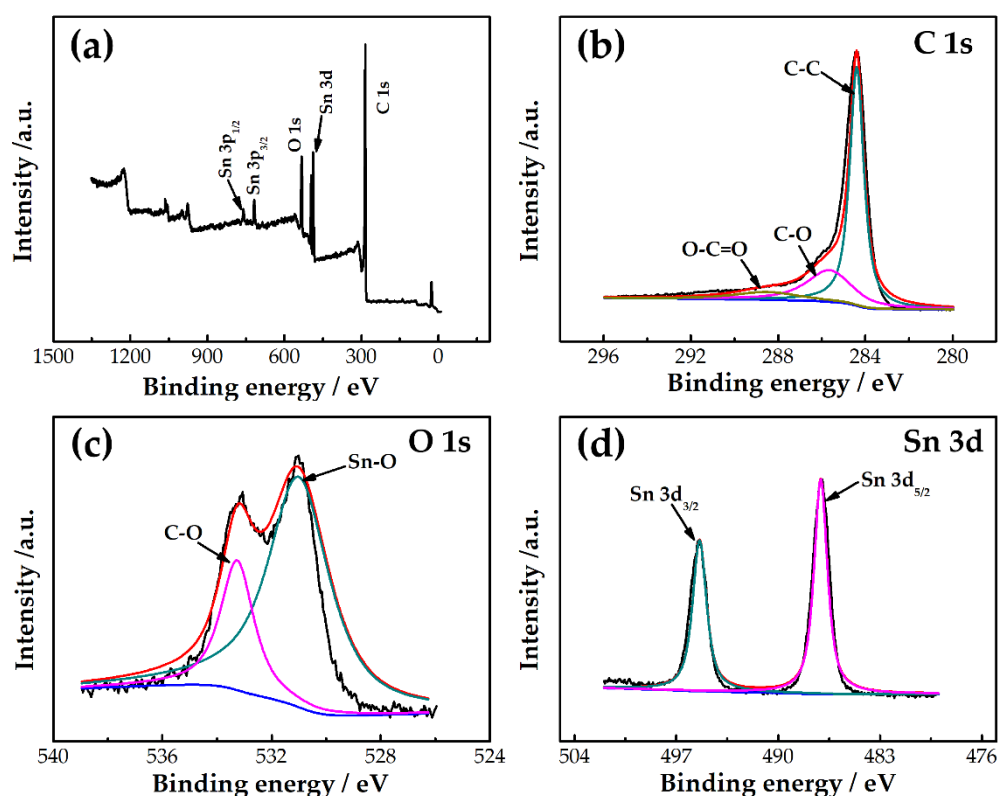
Figure 4. (**a**) XPS spectra of SnO_2/rGO, and the high-resolution XPS spectra of (**b**) C 1s, (**c**) O 1s, and (**d**) Sn 3d.

CV measurements were used to evaluate the effect of the samples on the electrocatalysis of a VO_2^+/VO^{2+} redox reaction. Figure 5a shows the CV curve of bare GCE. It indicates bare GCE without a catalysis for a VO_2^+/VO^{2+} redox reaction. It is beneficial to compare the electrochemical activity of the catalysts. The poor peak shape of SnO_2 is due to the poor electrical conductivity of SnO_2, which reduces the electrochemical reversibility of the electrode. The peak shape of GO is better than that of SnO_2, indicating the advantages of GO. The electrochemical performance of SnO_2/rGO composite is better than those of both GO and SnO_2. The composite has the synergistic effect of the good electrical conductivity of rGO and the good catalytic property of SnO_2. Moreover, it can be seen that the peak current of the SnO_2/rGO electrode (oxidation: 2.59 mA, reduction: 1.19 mA) is the largest, which again shows that SnO_2/rGO has a good electrochemical activity for a VO_2^+/VO^{2+} redox reaction.
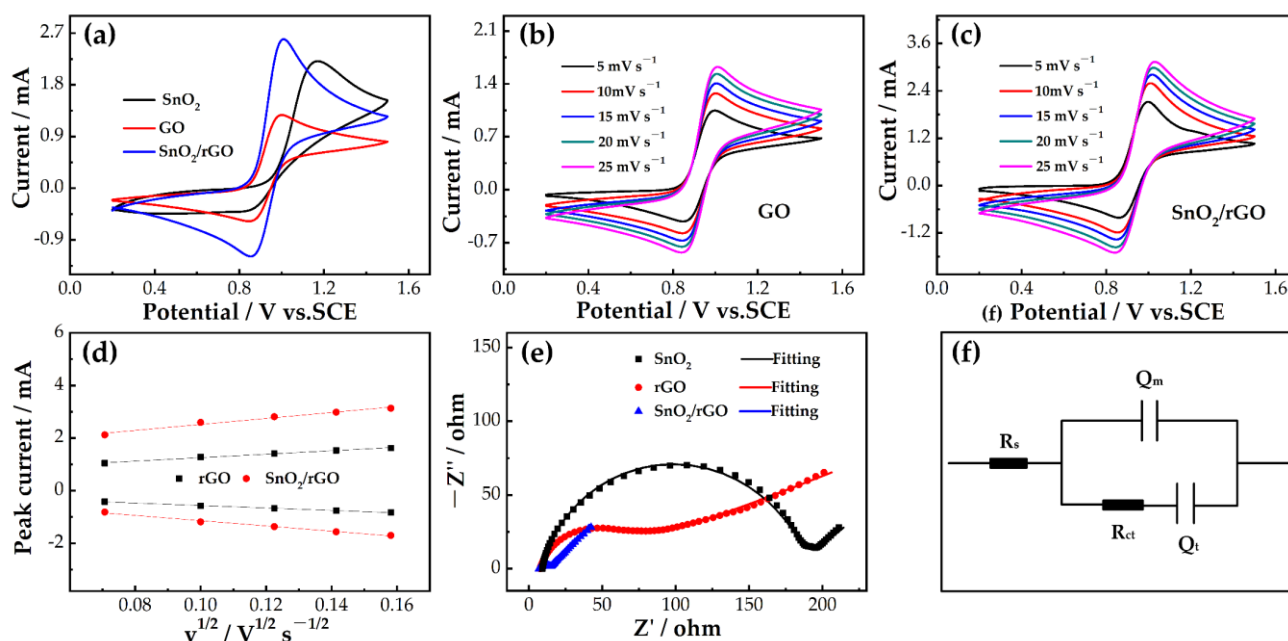
Figure 5. (**a**) CV curves for SnO_2, GO, and SnO_2/rGO in 1.6 M VO^{2+} + 3.0 M H_2SO_4 at a scan rate of 10 mV s^{-1}; (**b**) CVs for GO; (**c**) CVs for SnO_2/rGO; (**d**) CVs at different scan rates (5–25 mV s^{-1}) in 1.6 M VO^{2+} + 3.0 M H_2SO_4, and plots of the redox peak current versus the square root of the scan rate for GO and SnO_2/rGO electrodes; (**e**) Nyquist plots for SnO_2, GO, and SnO_2/rGO in 1.6 M VO^{2+} + 3.0 M H_2SO_4 at 0.85 V; (**f**) simplified electrical equivalent circuit fitting with Nyquist plots.

Figure 5b,c show the CVs of GO and SnO_2/rGO. As shown in the figure, with the change of the scan rate, the redox peak current also moves up and down. At a larger scan rate, the difference between the oxidation peak potential and the reduction peak potential gradually increases. Figure 5d depicts the relationship between the redox peak current and the square root of the scan rate. It is clear that there is a proportional relationship between the peak current and the square root of the scan rate, indicating that the reaction is controlled by the diffusion process [50]. The slope of SnO_2/rGO is higher than that of GO, which may be due to the fact that SnO_2/rGO has a better catalytic effect, so that the concentration difference on the electrode surface is larger.

To further explore the electrocatalytic property of the samples for redox reaction, we performed an EIS test. Figure 5e displays the Nyquist plots of the positive electrodes of SnO_2, GO, and SnO_2/rGO. In the Nyquist diagram, a semicircle appears at the high frequency region and a line appears at the low frequency region. This means that the VO_2^+/VO^{2+} electrode reaction is jointly governed by charge and mass transfer processes [51,52]. Figure 5f shows a simplified equivalent circuit diagram conforming to a Nyquist diagram.

The corresponding fitting electrochemical parameters of three samples are shown in Table 1. The ohmic resistance (R_s) of SnO_2/rGO and GO is smaller than that of SnO_2. In addition, the charge transfer resistance (R_{ct}) indicates that SnO_2/rGO < GO < SnO_2, which means that SnO_2/rGO has the lowest R_{ct}. The order of electrical double layer capacitance (Q_m) is SnO_2 < SnO_2/rGO < GO. GO has the highest Q_m because of a large number of hydrophilic groups on its surface. However, after calcination at high temperature, the hydrophilic groups of the composite are reduced and the Q_m is reduced. SnO_2 has the lowest Q_m because it has no hydrophilic groups on its surface. The order of diffusion capacitance (Q_t) is SnO_2 < GO < SnO_2/rGO. This may be due to the comprehensive effect of electrocatalysis and surface changes. The increase of Q_m can promote the charge migration of a VO_2^+/VO^{2+} reaction, and the increase of Q_t can accelerate the diffusion of VO_2^+/VO^{2+} ions on the electrode.

Table 1. Corresponding fitting electrochemical parameters for SnO_2, GO, and SnO_2/rGO.

| Sample	R_s/Ω	Q_m		R_{ct}/Ω	Q_t	
		Y_0	n_0		Y_1	n_1
GO	7.771	6.43×10^{-3}	0.24	37.4	2.86×10^{-5}	0.859
SnO_2	8.947	3.12×10^{-2}	0.48	177.5	3.08×10^{-5}	0.856
SnO_2/rGO	7.001	3.14×10^{-2}	0.53	7.41	4.95×10^{-4}	0.663

To explore the influence of the samples on the electrocatalysis of the V^{2+}/V^{3+} reaction, we carried out a CV test. Figure 6a displays the CV curves of GO and SnO_2/rGO in the 1.6 M V^{3+} + 3.0 M H_2SO_4, which indicate that SnO_2/rGO has a higher redox peak current than GO. The oxidation peak current of SnO_2/rGO can reach 1.56 mA, which is more than twice as high as that of GO (0.73 mA). The reduction peak current of SnO_2/rGO (2.82 mA) is 1.55 times higher than that of GO (1.82 mA). The results indicate that SnO_2/rGO also has superior electrocatalysis towards a V^{2+}/V^{3+} redox reaction. This is consistent with the results of the positive electrode. The EIS measurement for the negative couple was carried out to study the electrocatalytic activity. Figure 6b is the Nyquist diagram of the V^{2+}/V^{3+} reaction process of GO and SnO_2/rGO. It can be seen that the Nyquist diagram is similar to a semicircle at the high frequency region and a line in the low frequency region. This means the V^{2+}/V^{3+} reaction process is under co-control of the charge and mass transfer processes. Compared with GO, the smaller semicircle and higher slope of SnO_2/rGO mean lower charge transfer resistance and faster diffusion performance, which comes from the special structure of the SnO_2/rGO composite. It is the same as the positive EIS measurement analysis results.
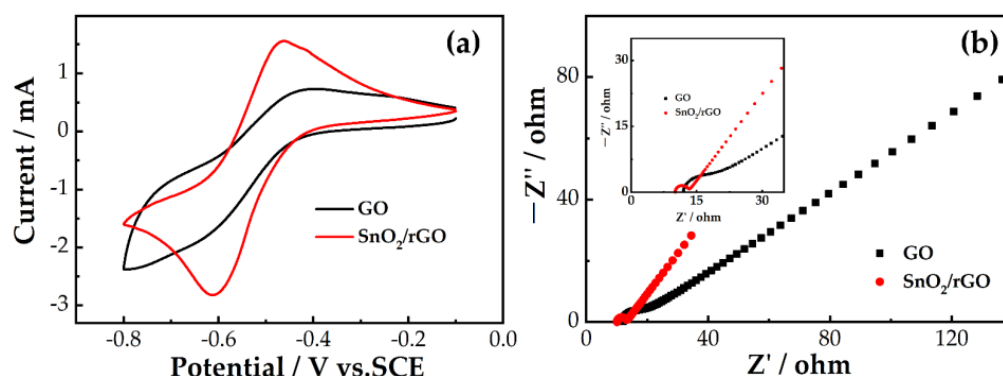
Figure 6. (**a**) CV curves; (**b**) CV curves at the scan rate of 10 mV s^{-1} and Nyquist plots for GO and SnO_2/rGO in 1.6 M V^{3+} + 3.0 M H_2SO_4 electrolyte.

Figure 7 shows the SEM images of pristine graphite felt and graphite felt modified with SnO_2/rGO. It is seen from Figure 7a,b that pristine graphite felt presents a clean and smooth surface. The diameter of the carbon fiber is 10–15 μm. It is observed in Figure 7c,d that graphite felt is uniformly coated with the SnO_2/rGO catalyst, which offers a larger reaction place and active sites for electrode reaction.
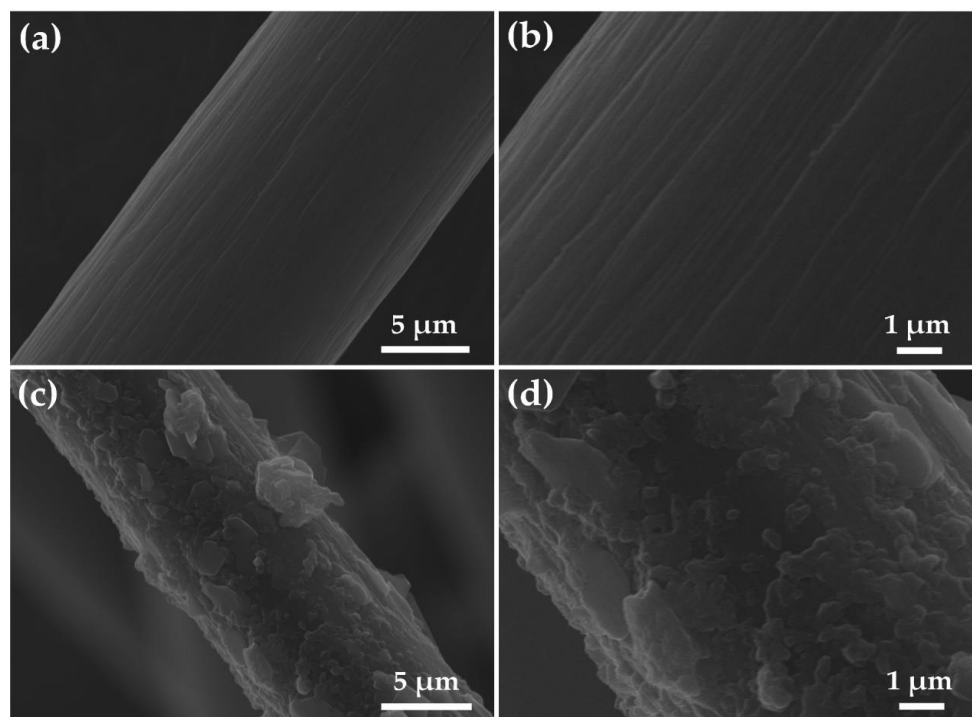
Figure 7. (**a**,**b**) SEM images of pristine graphite felt; (**c**,**d**) modified graphite felt with SnO_2/rGO.

Figure 8a displays the discharge capacity of the pristine and SnO_2/rGO modified cells at a different current density. It is observed that as the current density increases, the difference in discharge capacity between the two cells progressively increases. This result reflects that SnO_2/rGO has a good effect on increasing discharge capacity at a high current density. As a result, SnO_2/rGO can increase the reaction place and active site for electrode reaction, which increases the electrolyte utilization. In Figure 8b, the SnO_2/rGO cell exhibits a slightly lower than current efficiency (CE) as compared to the pristine cell. This is owing to a longer charge–discharge time of the SnO_2/rGO cell, and a more severe active substance penetration between two electrolytes in the SnO_2/rGO cell. In Figure 8c, there is an inversely proportional relation between voltage efficiency (VE) and current density. VE can reflect the cell polarization, including ohmic polarization, electrochemical polarization, and concentration polarization. SnO_2/rGO can reduce the electrochemical polarization and concentration polarization of the cell. The ohmic resistance of the two cells is comparable, as those two cells are comprised of the same components. The cell with SnO_2/rGO has a higher VE than the pristine one at 50–150 mA cm^{-2}. At 150 mA cm^{-2}, the modified cell shows an increase of 6.2% in VE compared to the pristine one (65.7%). This suggests that the SnO_2/rGO cell exhibits lower electrochemical polarization than the pristine one. As shown in Figure 8d, the energy efficiency (EE) is jointly affected by CE and VE. As the current density rises, the EE of both cells reduces. The SnO_2/rGO cell presents a greater EE than the pristine one. This indicates that the cell using SnO_2/rGO has a higher energy storage capacity. At 150 mA cm^{-2}, the EE of the modified cell is 69.8%, which is higher than that of the pristine cell (64.1%). These results indicate that the SnO_2/rGO modified cells can reduce the electrochemical polarization and have better energy storage performance. Figure 8e, f display the charge–discharge curves of two cells. It is seen from the comparison that the curves of the SnO_2/rGO modified cell exhibit a lower charge voltage and a higher discharge voltage than those of the pristine one. The reason is that the SnO_2/rGO composite material significantly boosts the redox reaction and reduces the polarization of the cell, suggesting that the SnO_2/rGO composite raises the energy density of the cell.
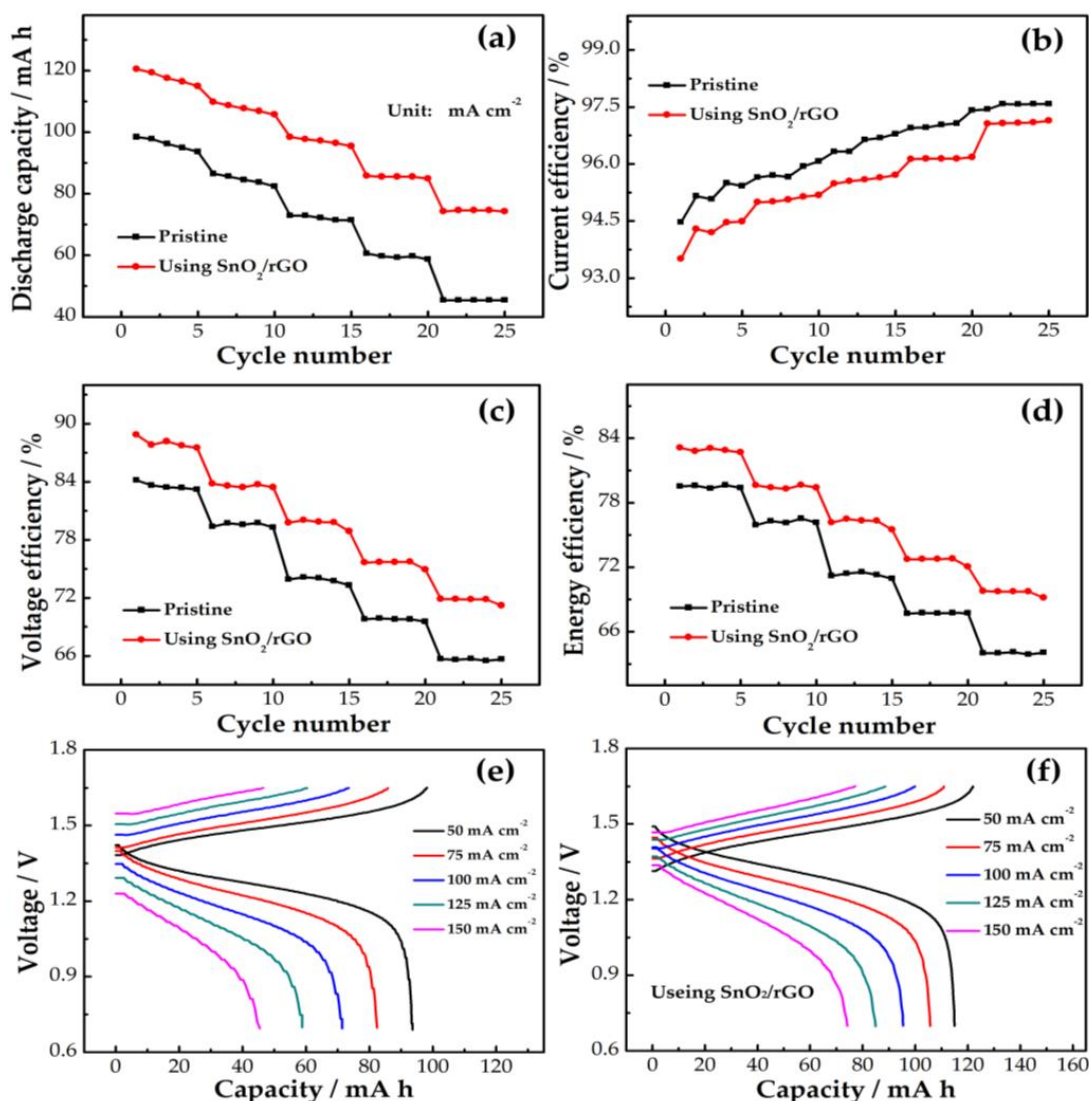
Figure 8. (**a**) Discharge capacity; (**b**) CE, (**c**) VE, and (**d**) EE of cells with and without SnO_2/rGO; (**e**) charge–discharge curves of pristine cell; (**f**) SnO_2/rGO modified cell at current density of 50–150 mA cm^{-2}.

4. Conclusions

In this work, an easy sol–gel approach was employed to a composite reduced graphene oxide, and SnO_2 was used as a bifunctional synergistic catalyst. The reduced graphene oxide as carbon support provides an adequate reaction place and fast electron transport due to its large surface area and fine conductivity. Moreover, SnO_2 has the intrinsic catalysis for a vanadium redox reaction. The strong interaction between the reduced graphene oxide and SnO_2 results in synergistical catalysis for redox reactions of VO_2^+/VO^{2+} and V^{2+}/V^{3+}, which systematically boosts the electrode reaction from diffusion, charge transfer, and electron transmission processes. Furthermore, SnO_2/rGO increases the electrolyte utilization of the cell and decreases the electrochemical polarization, resulting in higher discharge capacity and energy efficiency of the modified cell. At 150 mA cm^{-2}, the energy efficiency of the modified cell is increased to 69.8%, as compared to 64.1% in the pristine one.

Author Contributions: Conceptualization, Y.L. (Yongguang Liu), Y.J. and Y.L. (Yanrong Lv); Data curation, Z.H.; Formal analysis, Y.J.; Methodology, Y.L. (Yongguang Liu), Y.J. and Y.L. (Yanrong Lv); Resources, Z.H.; Software, Y.L. (Yongguang Liu), L.D. and L.W.; Writing—original draft, Y.L. (Yongguang Liu); Writing—review & editing, Y.J., Y.L. (Yanrong Lv) and Z.H. All authors have read and agreed to the published version of the manuscript.

Institutional Review Board Statement: Not applicable.

Informed Consent Statement: Not applicable.

Data Availability Statement: Not applicable.

Conflicts of Interest: The authors declare no conflict of interest.

Sample Availability: Samples of the compounds are NOT available from the authors.

References

1. Saloux, E.; Candanedo, J.A. Model-based predictive control to minimize primary energy use in a solar district heating system with seasonal thermal energy storage. *Appl. Energ.* **2021**, *291*, 116840. [CrossRef]
2. Wu, Y.H.; Tian, Z.N.; Yuan, S.F.; Qi, Z.Y.; Feng, Y.R.; Wang, Y.F.; Huang, R.; Zhao, Y.L.; Sun, J.H.; Zhao, W.; et al. Solar-driven self-powered alkaline seawater electrolysis via multifunctional earth-abundant heterostructures. *Chem. Eng. J.* **2021**, *411*, 127329. [CrossRef]
3. Zhang, S.Y.; Huang, Z.Q.; Wang, H.L.; Liu, R.K.; Cheng, C.; Guo, Z.Q.; Yu, X.Y.; He, G.C.; Fu, W. Separation of wolframite ore by froth flotation using a novel "crab" structure sebacoyl hydroxamic acid collector without $Pb(NO_3)_2$ activation. *Power Technol.* **2021**, *389*, 96–103. [CrossRef]
4. Huang, Z.Q.; Zhang, S.Y.; Wang, H.L.; Liu, R.K.; Cheng, C.; Liu, Z.W.; Guo, Z.Q.; Yu, X.Y.; He, G.C.; Ai, G.H.; et al. "Umbrella" structure trisiloxane surfactant: Synthesis and application for reverse flotation of phosphorite ore in phosphate fertilizer production. *J. Agric. Food Chem.* **2020**, *68*, 11114–11120. [CrossRef] [PubMed]
5. Kasaeian, A.; Bellos, E.; Shamaeizadeh, A.; Tzivanidis, C. Solar-driven polygeneration systems: Recent progress and outlook. *Appl. Energy* **2020**, *264*, 114764–114774. [CrossRef]
6. Khan, A.; Senthil, R.A.; Pan, J.; Osman, S.; Sun, Y.; Shu, X. A new biomass derived rod-like porous carbon from tea-waste as inexpensive and sustainable energy material for advanced supercapacitor application. *Electrochim. Acta* **2020**, *335*, 135588–135597. [CrossRef]
7. Kim, H.Y.; Joo, S.H. Recent advances in nanostructured intermetallic electrocatalysts for renewable energy conversion reactions. *J. Mater. Chem. A* **2020**, *8*, 8195–8217. [CrossRef]
8. Li, B.; Xue, J.; Han, C.; Liu, N.; Ma, K.X.; Zhang, R.C.; Wu, X.W.; Dai, L.; Wang, L.; He, Z.X. A hafnium oxide-coated dendrite-free zinc anode for rechargeable aqueous zinc-ion batteries. *J. Colloid Interface Sci.* **2021**, *599*, 467–475. [CrossRef]
9. Kou, Z.Y.; Lu, Y.; Miao, C.; Li, J.Q.; Liu, C.J.; Xiao, W. High-performance sandwiched hybrid solid electrolytes by coating polymer layers for all-solid-state lithium-ion batteries. *Rare Met.* **2021**, *40*, 3175–3184. [CrossRef]
10. Duburg, J.C.; Azizi, K.; Primdahl, S.; Hjuler, H.A.; Zanzola, E.; Schmidt, T.J.; Gubler, L. Composite polybenzimidazole membrane with high capacity retention for vanadium redox flow batteries. *Molecules* **2021**, *26*, 1679. [CrossRef] [PubMed]
11. Delgado, S.; Arevalo, M.D.; Pastor, E.; Garcia, G. Electrochemical reduction of carbon dioxide on graphene-based catalysts. *Molecules* **2021**, *26*, 572. [CrossRef]
12. Kim, S.; Kim, G.; Manthiram, A. A bifunctional hybrid electrocatalyst for oxygen reduction and oxygen evolution reactions: Nano-Co_3O_4-deposited $La_{0.5}Sr_{0.5}MnO_3$ via infiltration. *Molecules* **2021**, *26*, 277. [CrossRef] [PubMed]
13. Tang, F.; Gao, J.Y.; Ruan, Q.Y.; Wu, X.W.; Wu, X.S.; Zhang, T.; Liu, Z.X.; Xiang, Y.H.; He, Z.Q.; Wu, X.M. Graphene-wrapped MnO/C composites by MOFs-derived as cathode material for aqueous zinc ion batteries. *Electrochim. Acta* **2020**, *353*, 136570. [CrossRef]
14. Gao, J.W.; Xie, X.S.; Liang, S.Q.; Lu, B.A.; Zhou, J. Inorganic colloidal electrolyte for highly robust zinc-ion batteries. *Nano-Micro Lett.* **2021**, *13*, 69. [CrossRef] [PubMed]
15. Shan, L.T.; Wang, Y.R.; Liang, S.Q.; Tang, B.Y.; Yang, Y.Q.; Wang, Z.Q.; Lu, B.A.; Zhou, J. Interfacial adsorption-insertion mechanism induced by phase boundary toward better aqueous Zn-ion battery. *Infomat* **2021**. [CrossRef]
16. Chang, T.C.; Liu, Y.H.; Chen, M.L.; Tseng, C.C.; Lin, Y.S.; Huang, S.L. Cerium/ascorbic acid/iodine active species for redox flow energy storage battery. *Molecules* **2021**, *26*, 3443. [CrossRef] [PubMed]
17. Zhang, L.M.; Zhang, X.; Wang, J.; Seveno, D.; Fransaer, J.; Locquet, J.P.; Seo, J.W. Carbon nanotube fibers decorated with MnO_2 for wire-shaped supercapacitor. *Molecules* **2021**, *26*, 3479. [CrossRef]
18. Moghaddam, M.; Sepp, S.; Wiberg, C.; Bertei, A.; Rucci, A.; Peljo, P. Thermodynamics, charge transfer and practical considerations of solid boosters in redox flow batteries. *Molecules* **2021**, *26*, 2111. [CrossRef]
19. Wang, T.; Li, C.; Xie, X.; Lu, B.; He, Z.; Liang, S.; Zhou, J. Anode materials for aqueous zinc ion batteries: Mechanisms, properties, and perspectives. *Acs Nano* **2020**, *14*, 16321–16347. [CrossRef]
20. Liu, N.; Li, B.; He, Z.X.; Dai, L.; Wang, H.Y.; Wang, L. Recent advances and perspectives on vanadium- and manganese-based cathode materials for aqueous zinc ion batteries. *J. Energy Chem.* **2021**, *59*, 134–159. [CrossRef]

21. Baldinelli, A.; Barelli, L.; Bidini, G.; Discepoli, G. Economics of innovative high capacity-to-power energy storage technologies pointing at 100% renewable micro-grids. *J Energy Storage* **2020**, *28*, 101198. [CrossRef]
22. Busacca, C.; Di Blasi, O.; Giacoppo, G.; Briguglio, N.; Antonucci, V.; Di Blasi, A. High performance electrospun nickel manganite on carbon nanofibers electrode for vanadium redox flow battery. *Electrochim. Acta* **2020**, *355*, 136755. [CrossRef]
23. Chung, Y.; Noh, C.; Kwon, Y. Role of borate functionalized carbon nanotube catalyst for the performance improvement of vanadium redox flow battery. *J. Power Sources* **2019**, *438*, 227063. [CrossRef]
24. Divya, K.; Rana, D.; Saraswathi, M.; Nagendran, A. Custom-made sulfonated poly (vinylidene fluoride-co-hexafluoropropylene) nanocomposite membranes for vanadium redox flow battery applications. *Polym. Test* **2020**, *90*, 106685. [CrossRef]
25. Hu, G.J.; Jing, M.H.; Wang, D.W.; Sun, Z.H.; Xu, C.; Ren, W.C.; Cheng, H.M.; Yan, C.W.; Fan, X.Z.; Li, F. A gradient bi-functional graphene-based modified electrode for vanadium redox flow batteries. *Energy Storage Mater.* **2018**, *13*, 66–71. [CrossRef]
26. Lv, Y.R.; Han, C.; Zhu, Y.; Zhang, T.; Yao, S.; He, Z.X.; Dai, L.; Wang, L. Recent advances in metals and metal oxides as catalysts for vanadium redox flow battery: Properties, structures, and perspectives. *J. Mater. Sci. Technol.* **2021**, *75*, 96–109. [CrossRef]
27. Deng, Q.; Tian, Y.; Ding, P.; Yue, J.P.; Zeng, X.X.; Yin, Y.X.; Wu, X.W.; Lu, X.Y.; Guo, Y.G. Porous lamellar carbon assembled from *Bacillus mycoides* as high-performance electrode materials for vanadium redox flow batteries. *J. Power Sources* **2020**, *450*, 227633. [CrossRef]
28. Xia, L.; Zhang, Q.F.; Wu, C.; Liu, Y.R.; Ding, M.; Ye, J.Y.; Cheng, Y.H.; Jia, C.K. Graphene coated carbon felt as a high-performance electrode for all vanadium redox flow batteries. *Surf. Coat Tech.* **2019**, *358*, 153–158. [CrossRef]
29. Zhao, Y.; Ding, Y.; Li, Y.; Peng, L.; Byon, H.R.; Goodenough, J.B.; Yu, G. A chemistry and material perspective on lithium redox flow batteries towards high-density electrical energy storage. *Chem. Soc. Rev.* **2015**, *44*, 7968–7996. [CrossRef]
30. Li, W.Y.; Liu, J.G.; Yan, C.W. Multi-walled carbon nanotubes used as an electrode reaction catalyst for VO_2^+/VO_{2+} for a vanadium redox flow battery. *Carbon* **2011**, *49*, 3463–3470. [CrossRef]
31. He, Z.X.; Cheng, G.; Jiang, Y.Q.; Li, Y.H.; Zhu, J.; Meng, W.; Zhou, H.Z.; Dai, L.; Wang, L. Novel 2D porous carbon nanosheet derived from biomass: Ultrahigh porosity and excellent performances toward V^{2+}/V^{3+} redox reaction for vanadium redox flow battery. *Int. J. Hydrog. Energy* **2020**, *45*, 3959–3970. [CrossRef]
32. Cheng, D.; Tian, M.; Wang, B.; Zhang, J.; Chen, J.; Feng, X.; He, Z.; Dai, L.; Wang, L. One-step activation of high-graphitization N-doped porous biomass carbon as advanced catalyst for vanadium redox flow battery. *J. Colloid Interface Sci.* **2020**, *572*, 216–226. [CrossRef]
33. Wei, L.; Zhao, T.S.; Zeng, L.; Zhou, X.L.; Zeng, Y.K. Copper nanoparticle-deposited graphite felt electrodes for all vanadium redox flow batteries. *Appl. Energy* **2016**, *180*, 386–391. [CrossRef]
34. Jiang, Y.; Cheng, G.; Li, Y.; He, Z.; Zhu, J.; Meng, W.; Dai, L.; Wang, L. Promoting vanadium redox flow battery performance by ultra-uniform $ZrO_2@C$ from metal-organic framework. *Chem. Eng. J.* **2021**, *415*, 129014. [CrossRef]
35. Zhou, H.; Shen, Y.; Xi, J.; Qiu, X.; Chen, L. ZrO_2-nanoparticle-modified graphite felt: Bifunctional effects on vanadium flow batteries. *ACS Appl. Mater. Inter.* **2016**, *8*, 15369–15378. [CrossRef]
36. Vazquez-Galvan, J.; Flox, C.; Fabrega, C.; Ventosa, E.; Parra, A.; Andreu, T.; Morante, J.R. Hydrogen-treated rutile TiO_2 shell in graphite-core structure as a negative electrode for high-performance vanadium redox flow batteries. *ChemSusChem* **2017**, *10*, 2089–2098. [CrossRef] [PubMed]
37. Bayeh, A.W.; Lin, G.-Y.; Chang, Y.-C.; Kabtamu, D.M.; Chen, G.-C.; Chen, H.-Y.; Wang, K.-C.; Wang, Y.-M.; Chiang, T.-C.; Huang, H.-C.; et al. Oxygen-vacancy-rich cubic CeO_2 nanowires as catalysts for vanadium redox flow batteries. *ACS Sustain. Chem. Eng.* **2020**, *8*, 16757–16765. [CrossRef]
38. Bayeh, A.W.; Kabtamu, D.M.; Chang, Y.-C.; Chen, G.-C.; Chen, H.-Y.; Liu, T.-R.; Wondimu, T.H.; Wang, K.-C.; Wang, C.-H. Hydrogen-treated defect-rich $W_{18}O_{49}$ nanowires modified graphite felt as high-performance electrode for vanadium redox flow battery. *ACS Appl. Energy Mater.* **2019**, *2*, 2541–2551. [CrossRef]
39. Mehboob, S.; Ali, G.; Shin, H.-J.; Hwang, J.; Abbas, S.; Chung, K.Y.; Ha, H.Y. Enhancing the performance of all-vanadium redox flow batteries by decorating carbon felt electrodes with SnO_2 nanoparticles. *Appl. Energy* **2018**, *229*, 910–921. [CrossRef]
40. Wei, L.; Xiong, C.; Jiang, H.R.; Fan, X.Z.; Zhao, T.S. Highly catalytic hollow $Ti_3C_2T_x$ MXene spheres decorated graphite felt electrode for vanadium redox flow batteries. *Energy Storage Mater.* **2020**, *25*, 885–892. [CrossRef]
41. Xue, J.; Jiang, Y.; Zhang, Z.; Zhang, T.; He, Z. A novel catalyst of titanium boride toward V^{3+}/V^{2+} redox reaction for vanadium redox flow battery. *J. Alloy. Compd.* **2021**, *875*, 159915. [CrossRef]
42. Tz, A.; Yj, A.; Zz, A.; Jing, X.A.; Yl, A.; Yl, A.; Zc, B.; Zx, B.; Zl, B.; Lei, D. Zirconium boride as a novel negative catalyst for vanadium redox flow battery. *Ceram. Int.* **2021**, *47*, 20276–20285.
43. Ji, Y.; Li, J.L.; Li, S.F.Y. Synergistic effect of the bifunctional polydopamin Mn_3O_4 composite electrocatalyst for vanadium redox flow batteries. *J. Mater. Chem. A* **2017**, *5*, 15154–15166. [CrossRef]
44. Zhang, R.; Li, K.; Ren, S.; Chen, J.; Feng, X.; Jiang, Y.; He, Z.; Dai, L.; Wang, L. Sb-doped SnO_2 nanoparticle-modified carbon paper as a superior electrode for a vanadium redox flow battery. *Appl. Surf. Sci.* **2020**, *526*, 146685–146695. [CrossRef]
45. Choi, M.S.; Mirzaei, A.; Na, H.G.; Kim, S.; Kim, D.E.; Lee, K.H.; Jin, C.; Choi, S.W. Facile and fast decoration of SnO_2 nanowires with Pd embedded SnO_{2-x} nanoparticles for selective NO_2 gas sensing. *Sens. Actuat. B Chem.* **2021**, *340*, 129984. [CrossRef]
46. Ejigu, A.; Edwards, M.; Walsh, D.A. Synergistic catalyst-support interactions in a graphene-Mn_3O_4 electrocatalyst for vanadium redox flow batteries. *ACS Catal.* **2015**, *5*, 7122–7130. [CrossRef]

47. Xu, S.; Liu, J.; Xue, Y.; Wu, T.; Zhang, Z. Appropriate conditions for preparing few-layered graphene oxide and reduced graphene oxide. *Fuller. Nanotub. Carbon Nanostruct.* **2017**, *25*, 40–46. [CrossRef]

48. Yu, X.F.; Wu, Q.B.; Zhang, H.Y.; Zeng, G.X.; Li, W.W.; Qian, Y.N.; Li, Y.; Yang, G.Q.; Chen, M.Y. Investigation on synthesis, stability, and thermal conductivity properties of water-based SnO_2/reduced graphene oxide nanofluids. *Materials* **2018**, *11*, 38. [CrossRef] [PubMed]

49. Li, G.D.; Shen, Y.B.; Zhou, P.F.; Hao, F.L.; Fang, P.; Wei, D.Z.; Meng, D.; San, X.G. Design and application of highly responsive and selective rGO-SnO2 nanocomposites for NO2 monitoring. *Mater. Charact.* **2020**, *163*, 110284. [CrossRef]

50. Li, K.; Jiang, Y.Q.; Zhang, R.C.; Ren, S.Z.; Feng, X.J.; Xue, J.; Zhang, T.X.; Zhang, Z.X.; He, Z.X.; Dai, L.; et al. Oxygen vacancy and size controlling endow tin dioxide with remarked electrocatalytic performances towards vanadium redox reactions. *Colloid Surf. A* **2020**, *602*, 125073. [CrossRef]

51. Han, P.X.; Wang, H.B.; Liu, Z.H.; Chen, X.A.; Ma, W.; Yao, J.H.; Zhu, Y.W.; Cui, G.L. Graphene oxide nanoplatelets as excellent electrochemical active materials for VO^{2+}/VO_2^+ and V^{2+}/V^{3+} redox couples for a vanadium redox flow battery. *Carbon* **2011**, *49*, 693–700. [CrossRef]

52. Yang, S.B.; Feng, X.L.; Zhi, L.J.; Cao, Q.A.; Maier, J.; Mullen, K. Nanographene-constructed hollow carbon spheres and their favorable electroactivity with respect to lithium storage. *Adv. Mater.* **2010**, *22*, 838. [CrossRef] [PubMed]